Research article

Genetic algorithm shape optimization to manipulate the nonlinear response of a clamped-clamped beam

Tushar Mollik [a], Ying Geng [b], Md Raf E Ul Shougat [a], Timothy Fitzgerald [c], Edmon Perkins [a],*

[a] LAB2701, Department of Mechanical & Aerospace Engineering, North Carolina State University, Raleigh, NC 27695, United States of America
[b] LAB2701, Atwood, OK 74827, United States of America
[c] Department of Mechanical Engineering, Gonzaga University, Spokane, WA 99258, United States of America

ARTICLE INFO

ABSTRACT

Dynamical systems, which are described by differential equations, can have an enhanced response because of their nonlinearity. As one example, the Duffing oscillator can exhibit multiple stable vibratory states for some external forcing frequencies. Although discrete systems that are described by ordinary differential equations have helped to build fundamental groundwork, further efforts are needed in order to tailor nonlinearity into distributed parameter, continuous systems, which are described by partial differential equations. To modify the nonlinear response of continuous systems, topology optimization can be used to change the shape of the mechanical system. While topology optimization is well-developed for linear systems, less work has been pursued to optimize the nonlinear vibratory response of continuous systems. In this paper, a genetic algorithm implementation of shape optimization for continuous systems is described. The method is very general, with flexible objective functions and very few assumptions; it is applicable to any continuous system. As a case study, a clamped-clamped beam is optimized to have a more nonlinear or less nonlinear vibratory response. This genetic algorithm implementation of shape optimization could provide a tool to improve the performance of many continuous structures, including MEMS sensors, actuators, and macroscale civil structures.

1. Introduction

Nonlinearity can enhance the response of dynamical systems, such as energy harvesting [1, 2] and synchronization [3]. Distributed parameter systems possess a rich set of dynamics, with nonlinearities that could be harnessed with topology optimization techniques. For instance, a network of coupled mechanical oscillators can work as an inherent distributed sensing and computing system [4]. At low energy levels, a clamped-clamped beam can have a linear behavior; at intermediate energy levels, the response has the same qualitative shape as the Duffing equation [5]; at high energy levels, apart from Duffing oscillator behavior, modal coupling can result in a more complicated frequency responses [6, 7]. Although a relatively simple system, a hinged-clamped beam can have four stable dynamic solutions and three unstable dynamic solutions at some frequencies [8]. Such rich dynamics could enable new noise-enhanced responses that could be utilized for sensors, actuators, and civil structures. However, distributed parameter systems are described by partial differential equations (PDEs), which makes it

more complicated to control their dynamic response. In essence, simple, prototype systems are easy to tune, since the ordinary differential equations (ODEs) have a finite number of parameters to adjust. Although they possess a rich set of dynamics, distributed parameter systems are difficult to tune; a PDE-governed system has an infinite number of parameters to adjust.

Topology & shape optimization are important tools to unlock the potential of 3D printing [9]. Topology optimization is a mathematical process, in which an iterative method is used to find the optimal geometry of a structure [10]. Shape optimization is a subset of topology optimization, in which only the boundary of the object is modified; it is often used for static problems or linear vibration problems. They have classically been used to minimize the material of a given part, while maintaining the necessary strength. This is especially important for trusses [11, 12, 13, 14]. Some early work was pursued to take large displacements and nonlinearity into account using the Method of Moving Asymptotes (MMA), in order to optimize compliant mechanisms [15]. Equivalent static loads were used to optimize the shape of a non-

linear structure by converting the problem to a linear static response optimization and performing classical topology optimization [16].

Most work on topology optimization uses the Solid Isotropic Material with Penalisation (SIMP) method, which structures the problem as a gradient-based formulation [17], or an Evolutionary Structural Optimization approach, which uses a non-gradient-based formulation [18]. An Evolutionary Structural Optimization approach has also been used with shape optimization [19]. In the usual formulations, these methods pose the problem as a finite element problem where each unit cell can be void or filled, and the optimization routine decides how to fill each individual cell. Some other interesting optimization approaches have also been proposed. For instance, a genetic algorithm is used to build grippers by using a "library" of compliant building blocks [20]. In another genetic algorithm optimization scheme, a skeleton of the structure defines the underlying connectivity of a structural continuum together with segments of material surrounding the skeleton [21]. Similar multi-objective design methods have been used in optimization of several nonlinear geometric structures considering design constraints [22, 23, 24, 25]. These methods circumvent the costly issue of optimizing each individual cell in the finite element formulation. In a heuristic method called Proportional Topology Optimization, the design variables are assigned to finite elements proportionally to the value of stress in the stress-constrained problem and compliance in the minimum compliance problem [26]. A convolutional neural network [27] and a machine-learning approach [28] have been used to increase the speed of the optimization procedure. Instead of optimizing the material distribution of each cell of the entire FEM, the material distribution of a lattice structure can be used, which significantly reduces the computational cost of the optimization [29, 30]. This lattice structure is well-suited for 3D printing applications. For MEMS devices, shape optimization has been performed to enhance the performance of comb drives [31, 32], and topology optimization has been used to find the optimal topology of grippers [33] and resonators [34]. Topology optimization has been used to optimize the reliability of MEMS devices [35]. It should be noted that the Covariance Matrix Adaptation Evolution Strategy is an evolutionary optimization strategy that is similar to the genetic algorithm, and it has been applied to a MEMS resonator system [36]; although the optimization problem is nonlinear, the nonlinearity of the system's response was not considered. The genetic algorithm has also been applied to optimize the nonlinear vibratory response of a MEMS vibratory energy harvester, but the shape of the harvester was not considered in the optimization procedure [37].

For linear vibrations, the natural frequency of the system can be optimized using shape optimization [31] or topology optimization [29, 30]. A binary level set framework was used for frequency optimization of drum and structure shape in [38, 39]. Through modification of a structure's spatial material distribution, topology optimization presents a unique opportunity to overcome the barrier of tuning the nonlinearity of distributed parameter systems to harness their rich dynamics. For strongly nonlinear systems, recent advances have allowed for application of topology optimization [40, 41] and shape optimization [42, 43] to nonlinear vibratory systems. Importantly, incremental harmonic balance was used to formulate a topology optimization scheme, in order to modify quadratic and cubic nonlinearities of a clamped-clamped beam [41]. The nonlinear normal modes for a clamped-clamped beam and a coupled-mode resonator were calculated to modify the cubic nonlinearity and modal coupling, respectively [44]. This work has been experimentally validated with a MEMS implementation for shape optimization [45]. These useful papers lay a basis to build further topology optimization implementations to tune nonlinearities in distributed parameter systems.

Gradient-based approaches, such as the ones mentioned above, are computationally efficient. However, these gradient-based approaches cannot readily be applied to general nonlinear systems. For this reason, this paper presents a genetic algorithm implementation for shape optimization to tune the nonlinear stiffness of a continuous system. This is a general method that can be used to optimize any continuous system. In this parallelizable formulation, the nonlinear force-displacement curves of different beams are used to optimize the shape.

For the shape optimization presented in this manuscript, a unique genetic algorithm implementation is formulated to optimize the shape of a beam. In this formulation, relatively sparse control points are used with a piecewise cubic Hermite interpolating polynomial spline to create one quarter of a beam. This spline was chosen because it avoids overshooting the control points, which would create an unduly wavy beam shape. Overshooting is a significant issue, since it could also cause some combinations of control points that are within the chosen bounds but produce a spline that is outside of these chosen bounds. This spline is constructed to have a slope of zero at the clamped end and at the midpoint of the beam to preserve smoothness at the center. The crossover step in the genetic algorithm is formulated to preserve local relationships between the control points, as these local relationships between adjacent points are likely important in creating a macroscale nonlinear stiffness of the beam. The force-displacement curve is found using a Total Lagrangian geometrically exact nonlinear finite element scheme. In addition to this unique formulation that requires few control points and preserves local relationships between these control points, the objective functions used here are somewhat non-standard. The results are verified using time-marching with the finite element method in Section 4. It is found that the non-standard objective functions did indeed produce more hysteresis in the case of the nonlinear objective function and less hysteresis in the case of the linear objective function.

As an example case, two clamped-clamped beams were optimized to have a more nonlinear and a more linear response as compared to its rectangular prism counterpart. The force-displacement curves and frequency response curves are determined through finite element analysis of the beam shapes. Instead of optimizing the material distribution of each cell of the beams, a spline is used to describe the boundary of a clamped-clamped beam. Parametric control points were tuned with the genetic algorithm to optimize the shape of the spline. For thin structures, this prevents holes from forming inside the structure, which could be difficult to fabricate and could cause localized vibratory modes to form. It also decreases the parameter space that is being optimized.

2. Finite element formulation

The description of the body is performed using a Total Lagrangian geometrically exact nonlinear finite element scheme, with a consistent mass matrix. This means that there is no approximation to the kinematics of the strain. The resulting nonlinear equations are solved to equilibrium iteratively. The FEM formulation is implemented in MATLAB, following the assembly procedures of Hughes [46], while nonlinear stress and strain measures are built following Belytschko et al. [47].

The open-source meshing program, GMSH [48], is used to generate the nodal locations and element connectivity. In this formulation, all volume elements are isoparametric 27-node hexahedra. Fully quadratic elements are chosen to avoid any issues with locking due to bending. Standard Gauss-Legendre quadrature is used to consistently integrate the internal forces, stiffness matrix, and mass matrix.

The material law chosen is inspired by [49, 50], and this law can be viewed as a generalization of engineering stress-strain with invariance to rigid-body motion. The polar decomposition of the deformation gradient, $\mathbf{F} = \mathbf{RU}$, is one method to build the pure stretch tensor, $\mathbf{U}$ [51]. In structural mechanics, co-rotational methods are employed as a local frame to decompose rigid motion from deformation. The polar decomposition provides this in a point-wise continuous fashion through each element. The benefit is an elastic law that is *linear-with-respect-to-stretch* as opposed to other geometrically exact laws, such as the Saint Venant–Kirchhoff model, that are not.

The Biot (or Jaumann) strain is defined in eq. (1) as:

$$\mathbf{L} = \mathbf{U} - \mathbf{I}. \tag{1}$$

The hyperelastic material law is based on Hooke's Law for an isotropic material, except the strain is replaced with $\mathbf{L}$, and the stress is the work-conjugate symmetric Biot stress $\mathbf{G}$. This modified Hooke's Law is defined as eq. (2), which is stated in terms of Young's Modulus, E, and Poisson's Ratio, ν, as:

$$\mathbf{G} = \frac{E}{(1+\nu)}\mathbf{L} + \frac{E\nu}{(1+\nu)(1-2\nu)}\mathrm{tr}(\mathbf{L})\mathbf{I}. \tag{2}$$

Relating it to the 2nd Piola-Kirchhoff stress tensor, $\mathbf{S}$, is needed, since the latter is used throughout the FEM solver. In general, the stresses can be related in the following eq. (3) [52]:

$$\mathbf{G} = \frac{1}{2}(\mathbf{US} + \mathbf{SU}) \tag{3}$$

Since the material is isotropic, it can be simplified as in eq. (4), which gives the explicit relation:

$$\mathbf{S} = \mathbf{GU}^{-1} = \mathbf{U}^{-1}\mathbf{G}. \tag{4}$$

The 2nd Piola-Kirchhoff stress tensor is then used in the formulation of Belytschko *et al.* [47] to build the internal forces, $\mathbf{f}_{int}$, of the system's equations of motion, eq. (5):

$$\mathbf{M}\ddot{\mathbf{q}}(t) + \mathbf{D}\dot{\mathbf{q}}(t) + \mathbf{f}_{int}(t) = \mathbf{f}_{ext}(t) \tag{5}$$

where $\mathbf{M}$ is the consistent mass matrix, $\mathbf{D}$ is an optional damping matrix, and $\mathbf{f}_{ext}(t)$ is the vector of external loads and prescribed-displacement boundary conditions. The degrees of freedom, namely the displacements of each node, are contained in $\mathbf{q}(t)$. It should be noted that eq. (5) is the spatially-discretized formulation of the beam, which is a simplification of this system, as the beam is described by a partial differential equation.

The linearization of these equations, needed when using Newton-Raphson schemes, can be involved. The non-typical part is how to compute the derivative of $\mathbf{U}$ with respect to the degrees of freedom. Chen and Wheeler [53] provide a method for computing the derivative of $\mathbf{U}$ with respect to $\mathbf{F}$, which can then be used via a chain rule to compute the needed derivatives as shown in eq. (6):

$$\frac{\partial \mathbf{U}}{\partial q_k} = \frac{\partial \mathbf{U}}{\partial \mathbf{F}} : \frac{\partial \mathbf{F}}{\partial q_k} = \mathbf{R}^T \frac{\partial \mathbf{F}}{\partial q_k} - \frac{1}{\det(\mathbf{Y})}\mathbf{Y}\left(\mathbf{R}^T\frac{\partial \mathbf{F}}{\partial q_k} - \frac{\partial \mathbf{F}^T}{\partial q_k}\mathbf{R}\right)\mathbf{YU} \tag{6}$$

where $\mathbf{Y} = \mathrm{tr}(\mathbf{U})\mathbf{I} - \mathbf{U}$, and the colon : is a double contraction [51] between the rank-4 tensor, $\frac{\partial \mathbf{U}}{\partial \mathbf{F}}$, and the rank-2 tensor, $\frac{\partial \mathbf{F}}{\partial q_k}$.

Classical load-stepping [47] is done on the static problem ($\ddot{\mathbf{q}}(t) \to \mathbf{0}$, $\dot{\mathbf{q}}(t) \to \mathbf{0}$). It begins with the unloaded system at rest, and then a small fraction of the desired load is placed on the body. Equilibrium of the equations of motion is achieved via a Newton-Raphson method to a desired tolerance. This static load-stepping is used in the optimization step as a means to approximate the shape of the desired standing wave in a computationally inexpensive manner.

The dynamics of the optimized configurations are studied by producing frequency-amplitude plots of the forced response. These are generated via a simple frequency sweep, in a manner that mimics a physical experiment and determines the stable periodic motions. The Generalized-α method [54] was chosen as the time-marching scheme. This method was extended to nonlinear systems [55, 56], and its properties are well-studied [57]. It is a single-parameter method, which is a descendent of the classical Newmark method used throughout commercial FEM applications. The goal of this class of methods is to filter out high frequency oscillations and preserve low frequency information. The high frequency attenuation permits the step-size to be somewhat independent of the mesh size, otherwise Nyquist stability becomes dominant as meshes are refined. This implicit method permits an accurate simulation of the principal dynamics while taking time-steps that are quite large compared to the higher natural frequencies of the mesh.
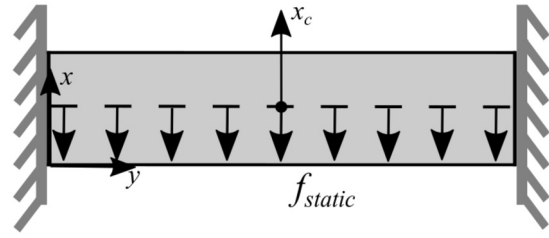

Fig. 1. Static load stepping. Load-stepping is used to find the force-displacement curves, where f_{static} is stepped through increments of 10^{-4} units, and this force is applied to all nodes at the geometric center of the beam. The beam's force-displacement relationship shown here is for a 1:10:100 rectangular prismatic beam. The x-axis is in the direction of the width of the beam, the y-axis is in the direction of the length of the beam, and the z-axis is in the direction of the thickness of the beam. The x_c-axis is at the center of the beam.

3. Genetic algorithm implementation of topology optimization

The genetic algorithm implementation described in this section do not require a gradient to be computed from the partial differential equation. The beams involved in this optimization are completely described by a set of control points, whose limits are described in Eq (12). The FEM formulation provided in the previous section is used to numerically obtain the linear and nonlinear stiffness terms for each beam described by a specific set of control points. These stiffness terms are then used to evaluate an objective function, which is minimized during the optimization routine.

The beams studied here have a ratio of 1:10:100 for the thickness, width, and length, respectively. The finite element formulation described in Section 2 was used for both the load-stepping simulations in this section and the time history simulations to find the hysteresis plots in the next section. The configuration of the load-stepping scheme is described in Fig. 1.

The simulations used in the genetic algorithm were run in parallel using the *Henry2* high performance computing cluster at North Carolina State University. The *Henry2* cluster is a heterogeneous cluster that includes state-of-the-art equipment, such as the newest CPUs, GPUs, and networking architecture while maintaining older resources as long as feasible. The cluster is an Intel Xeon based Linux cluster, and compute nodes include a mix of several generations of Intel Xeon processors primarily in dual-socket blade servers. The FEM simulation of 1000 beams takes about 4 hours of wall time with this parallel architecture using this HPC.

3.1. Stiffness coefficients and objective functions

A polynomial containing 1st and 3rd order terms was used to curve fit the relationship between the applied force and the beam's displacement as a Duffing spring [58]:

$$f(x_c) = k_1 x_c^1 + k_3 x_c^3, \tag{7}$$

where x_c is the displacement of the center of the beam, k_1 and k_3 are the linear and nonlinear spring stiffness terms of the beam, respectively. This was chosen since the vibratory response of a clamped-clamped beam has the same qualitative shape as the Duffing equation [5]. The force and displacement data from the load-stepping simulation is fitted in Eq (7) to find the spring stiffness of the beam. Only 1st and 3rd terms were used, because 2nd, 4th, and 5th order terms were found to be approximately zero for the rectangular prism beam. If these other terms are included in the curve fit in the next section, they would converge to negative values, which effectively would over-estimate the cubic nonlinearity. For other systems with more complex nonlinearities, a similar reduced-order modeling procedure could be used to keep only terms that are significant in the curve fit of the original system. An example curve fitting is depicted in Fig. 2 for a rectangular prism beam. The best
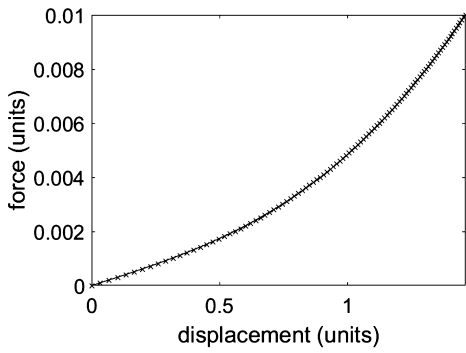
Fig. 2. Force-displacement relationship of rectangular prism beam. A polynomial was used to curve fit the relationship between the applied force and the beam's spring force, $f(x_c) = \bar{k}_1 x_c + \bar{k}_3 x_c^3$, where x_c is the displacement of the center of the beam. It was found that $\bar{k}_1 = 0.0030$ and $\bar{k}_3 = 0.0018$ for the rectangular prism beam. In the plot, the Xs correspond to numerical results, and the solid curve corresponds to the curve fit.
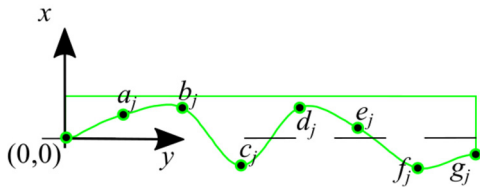

Fig. 3. Control points. Seven movable points, labeled a_j-g_j, are chosen from a uniform distribution. A *pchip* spline is then used to smoothly connect the points.

fit stiffness values are found to be $k_1 = 0.0030$ and $k_3 = 0.0018$ for the rectangular prism beam, which are plotted as dashed lines in Fig. 5. It should be noted that a clamped-clamped rectangular prism beam is sometimes approximated as a Duffing oscillator, as the nonlinear behavior is dominant in the force-displacement curve as can be seen in Fig. 2.

Two different single objective functions were explored, O_{linear} and $O_{Duffing}$:

$$O_{linear}(k_1, k_3) = -\sqrt{k_1^2} + \sqrt{k_3^2} \tag{8}$$

$$O_{Duffing}(k_1, k_3) = \sqrt{k_1^2} - \sqrt{k_3^2} \tag{9}$$

These objective functions are minimized in the optimization procedure. The first of these objective functions, Eq (8), was chosen to create a beam that behaves more linearly; this objective function tries to simultaneously minimize the Duffing nonlinear term and maximize the linear term in the beam's spring stiffness. The second of these objective functions, Eq (9), was chosen to create a beam that has a predominantly Duffing behavior; this objective function tries to maximize the Duffing nonlinear term and minimize the linear term in the beam's spring stiffness.

3.2. Beam shape definition and constraints

To create the beam shapes, seven control points are generated those define one quarter of the beam, as shown in Fig. 3. A piece-wise cubic Hermite interpolating polynomial spline was used to smoothly connect these seven movable control points, using *pchip* in MATLAB. Two constraints are applied explicitly to generate the control points:

$$x_0 = 0 \tag{10}$$

$$\frac{dx}{dy}\bigg|_{y=0,l/2} = 0 \tag{11}$$

The first constraint, Eq (10), sets the first control point to be fixed at the origin, where x_0 is the control point at $y = 0$. This, in turn, sets

a fixed width at the two ends, and the other portions of the beam can be optimized with respect to this width as a reference. The second constraint, Eq (11), defines a zero slope of the spline at the origin and at the center of the beam (control point g_j) to mitigate sharp angles. The control points were chosen randomly from a uniform distribution, with probability density function:

$$p_0(x) = \begin{cases} \frac{1}{b_0 - a_0} & \text{if } a_0 < x < b_0 \\ 0 & \text{if } x < a_0 \text{ or } x > b_0 \end{cases} \tag{12}$$

Here x is the x-value of the control point, $a_0 = -0.45$, and $b_0 = +0.45$. The control points are movable along the x-axis and equidistant along the y-axis.

To create a symmetric beam, the quarter beam shape was rotated 180° around the vertical axis, and the lower half of the beam was then rotated 180° about the horizontal axis as shown in Fig. 4. The horizontal mid-line of the beam is 0.5 units away from the origin in the positive x-direction. The value for a_0 and b_0 were chosen so that the beam would always have a minimal width of 0.1 and maximal width of 1.9.

3.3. Genetic algorithm

The genetic algorithm is an optimization method that is especially well-suited for problems that are not gradient-based. At every step for this topology optimization method, the control points defining the beam are kept within the limits described in Eq (12). The genetic algorithm optimization was performed as follows:

1. 1000 beams were simulated using the load-stepping method with different control points. This will be referred to as the zeroth generation, gen_0.
2. The desired objective function is used to quantify the 10 most optimal beams.
3. These 10 most optimal beams are used in the *crossover procedure* to find a new batch of beams. The crossover procedure is discussed below. This batch of beams created from this procedure are simulated as the ith generation crossover step, $gen_{i,cross}$.
4. The desired objective function is used to quantify the top 10% most optimal beams.
5. These top 10% most optimal beams are used in the *mutation procedure* to find a new batch of beams. The mutation procedure is discussed below. This batch of beams created from this procedure are simulated as the ith generation mutation step, $gen_{i,mut}$.
6. Steps 2-5 are repeated until an end condition is met, such as the objective function stops improving. Here, five generations were used.

3.4. Crossover procedure

For the crossover procedure for generation i, the control points for the ten most optimal beams were first written in a matrix, C_i, with control points $a_j - g_j$ for the jth beam, which is depicted in eq. (13):

$$C_i = \begin{bmatrix} a_1 & b_1 & c_1 & d_1 & e_1 & f_1 & g_1 \\ a_2 & b_2 & c_2 & d_2 & e_2 & f_2 & g_2 \\ a_3 & b_3 & c_3 & d_3 & e_3 & f_3 & g_3 \\ \vdots & \vdots & \vdots & \vdots & \vdots & \vdots & \vdots \\ a_{10} & b_{10} & c_{10} & d_{10} & e_{10} & f_{10} & g_{10} \end{bmatrix} \tag{13}$$

Next, the control points on one row of the matrix to the left of the vertical line are chosen; these points are then concatenated with the control points to the right of the vertical line. For example, in the matrix shown in eq. (14):, $[\mathbf{a_2}, \mathbf{b_2}]$ are concatenated with $[c_j, d_j, e_j, f_j, g_j]$ for $1 \leq j \leq 10$.
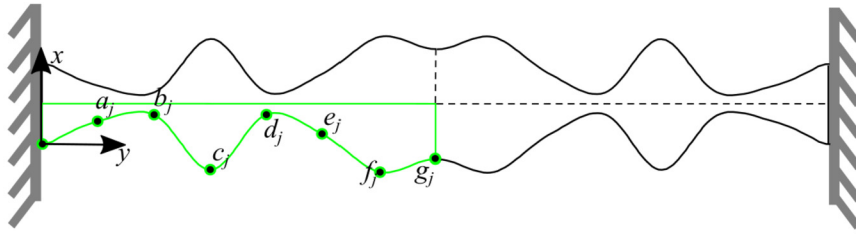
Fig. 4. Beam creation. The quarter section of the beam (green) is rotated around the vertical axis, and the lower half of the beam is rotated around the horizontal axis to create a symmetric beam.
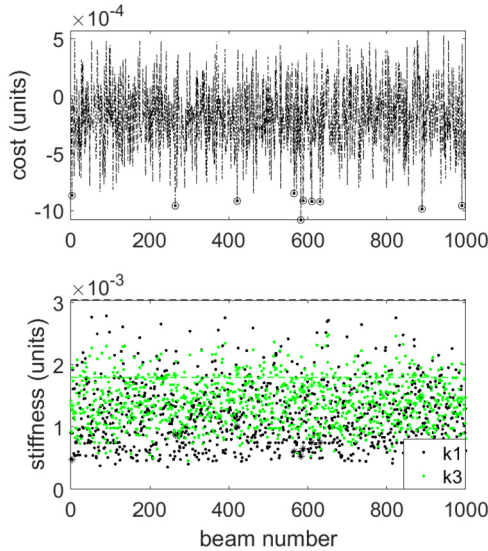

Fig. 5. Results for zeroth generation. For gen_0, 1000 beams with random control points were simulated. With varying control points, beams with different stiffness coefficients were created. In the top plot, Eq (9) was used as the objective function, and "cost" is the value of the objective function for each set of k_1 and k_3 values. The circles on the plot denote the ten most optimal beams, which are used in $gen_{1,cross}$. In the bottom plot, the dashed lines are the values of the stiffness coefficients for the rectangular prism beam, and the dots denote the stiffness coefficients for each of the 1000 beam. Black denotes the linear stiffness term, k_1, and green denotes the cubic stiffness term, k_3. The values of k_1 and k_3 are found by curve fitting the force displacement curve, such as the examples shown in Figs. 2, 7, and 8.

$$C_i = \begin{bmatrix} a_1 & b_1 & c_1 & d_1 & e_1 & f_1 & g_1 \\ \mathbf{a_2} & \mathbf{b_2} & c_2 & d_2 & e_2 & f_2 & g_2 \\ a_3 & b_3 & c_3 & d_3 & e_3 & f_3 & g_3 \\ \vdots & \vdots & \vdots & \vdots & \vdots & \vdots & \vdots \\ a_{10} & b_{10} & c_{10} & d_{10} & e_{10} & f_{10} & g_{10} \end{bmatrix} \quad (14)$$

To create all of the control points, the vertical line used to perform the crossover is moved from left to right across matrix C_i; in this way, there are six crossover positions. Likewise, the row used to perform the crossover is moved from top to bottom across matrix C_i; in this way, there are ten sets of control points created from each row per crossover. Thus, there is a total of 600 sets of control points created from this crossover procedure, of which 60 of them are the original ten sets of "parent" control points. 50 of these duplicates are then removed, leaving 550 sets of "children" control points. The ten original "parent" control point sets are also members of the new set of control point sets; this ensures that, if none of the "children" control point sets improved, the new generation would not be worse than the previous generation. The crossover procedure was devised in this way, so that portions of the beam remain unchanged during this procedure.
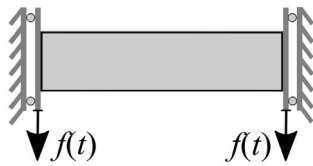
3.5. Mutation procedure

From the crossover procedure just discussed, the top 10% of the control point sets for the most optimal beams are then used in the mutation procedure. For the mutation procedure of generation i, the 55 control point sets are first written as a matrix, M_i, with control points $a_j - g_j$ for the jth beam, which is depicted in eq. (15):

$$M_i = \begin{bmatrix} a_1 & b_1 & c_1 & d_1 & e_1 & f_1 & g_1 \\ a_2 & b_2 & c_2 & d_2 & e_2 & f_2 & g_2 \\ a_3 & b_3 & c_3 & d_3 & e_3 & f_3 & g_3 \\ \vdots & \vdots & \vdots & \vdots & \vdots & \vdots & \vdots \\ a_{55} & b_{55} & c_{55} & d_{55} & e_{55} & f_{55} & g_{55} \end{bmatrix} \quad (15)$$

A random vector, $\vec{r} = [r_1, r_2, r_3, r_4, r_5, r_6, r_7]$, is then created. The r_k values are chosen randomly from a uniform distribution, with probability density function given by eq. (16):

$$p_i(x) = \begin{cases} \frac{1}{b_i - a_i} & \text{if } a_i < x < b_i \\ 0 & \text{if } x < a_i \text{ or } x > b_i \end{cases} \quad (16)$$

where $a_i = \frac{a_0}{2^i}$, and $b_i = \frac{b_0}{2^i}$. For each row of matrix M_i, nine new control point sets are created by adding nine different random vectors to that row; this results in 495 "children" control point sets from the 55 "parent" control point sets. The 55 original "parent" control point sets are also members of the new set of control point sets; this ensures that, if none of the "children" control point sets improved, the new generation would not be worse than the previous generation.

4. Results

The procedure described in Section 3 was repeated until a convergence criteria was met. In this case, the genetic algorithm was stopped when the best beam from generation i improved less than 2% as compared to the best beam in generation $i-1$. Two beams were created: the linear beam configuration has a stiffness that is dominated by the linear term, which was created by using objective function Eq (8), and the nonlinear beam configuration has a stiffness that is dominated by the Duffing term, which was created by using objective function Eq (9). It should be noted that for entire optimization procedure the minimum coefficient of determination of the curve fit was always near one ($min(R^2) > 0.997$). It was found that a coarse mesh was sufficient to capture the nonlinearity and produce sufficient solutions. The mesh has 30 elements in the length (y), two in the width (x), and one in the thickness (z) for a total of 915 nodes.

In addition, the finite element model described in Section 2 was used to simulate sinusoidal base excitation, depicted in Fig. 6. It should be noted that the direction of oscillation was the same direction as the distributed load applied in the load-stepping cases.

In the bottom-right portion of Figs. 7 and 8, the frequency-amplitude relationship for the linear beam configuration and the nonlinear beam configuration are shown, respectively. In addition, the frequency-amplitude relationship for the rectangular prism beam is also shown for comparison. In these numerical experiments, the frequency was quasi-statically increased so that the beam's response would follow the

Fig. 6. Dynamic loading. After the force-displacement curves are optimized, the dynamic response of the sinusoidally forced clamped-clamped beam is found. For the dynamic loading, $f(t) = a\sin(\Omega t)$, where a is the amplitude of the sinusoidal forcing and Ω is the forcing frequency.
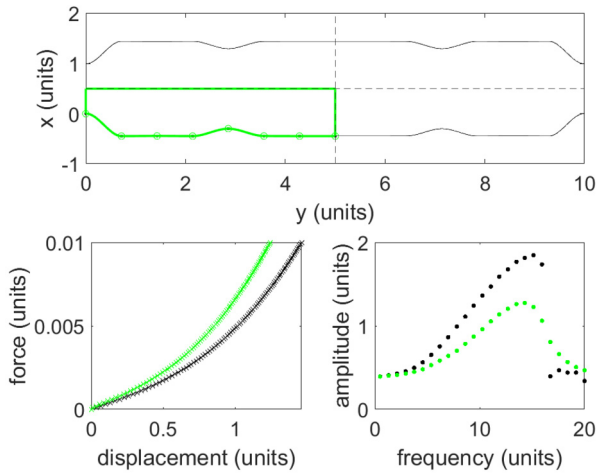

Fig. 7. Optimized linear beam configuration. Top: The linear beam configuration is shown, with control points $a = -0.450$, $b = -0.446$, $c = -0.450$, $d = -0.301$, $e = -0.448$, $f = -0.450$, $g = -0.450$. The green portion represents the quarter of the beam described by these control points, while the rest of the optimized beam is plotted in black. Bottom-left: The force-displacement curve of the linear beam configuration (green) and the rectangular prism beam (black). Bottom-right: The frequency-amplitude response of the linear beam configuration (green) and the rectangular beam (black), when the forcing amplitude is set to 0.4. Notice that the linear beam configuration has no noticeable jump in the frequency-amplitude plot, while the rectangular prism beam does. In the lower left plot, the Xs correspond to numerical results, and the solid curve corresponds to the curve fit.

stable branch of the frequency-amplitude curves, which are seen in the lower-left portions of Figs. 7 and 8. The "jump" in the beam's response happens near the termination point of a stable branch, while an unstable branch is not shown.

4.1. Linear beam configuration

When minimizing the objective function found in Eq (8), the topology optimization procedure produces the beam shape found in Fig. 7. Using the linear objective function, there was a 1.3% improvement from generation 4 to generation 5. This linear beam configuration is shown in the top portion of Fig. 7. The force-displacement curve is shown in the bottom-left portion of this figure. For the rectangular prism beam, $k_1 = 0.0030$ and $k_3 = 0.0018$. For the linear beam configuration, $k_1 = 0.0038$ and $k_3 = 0.0027$. Both the linear and cubic stiffnesses increased.

In Fig. 7, the dynamic forcing amplitude was set to $a = 0.04$; for this large amplitude, the rectangular beam has a noticeable jump in the amplitude at a frequency of approximately 15 rad/s. This is expected, since a clamped-clamped rectangular beam has a cubic stiffness term. However, the linear beam configuration, even for this large amplitude of forcing, does not exhibit a jump in the amplitude as the frequency is changed.
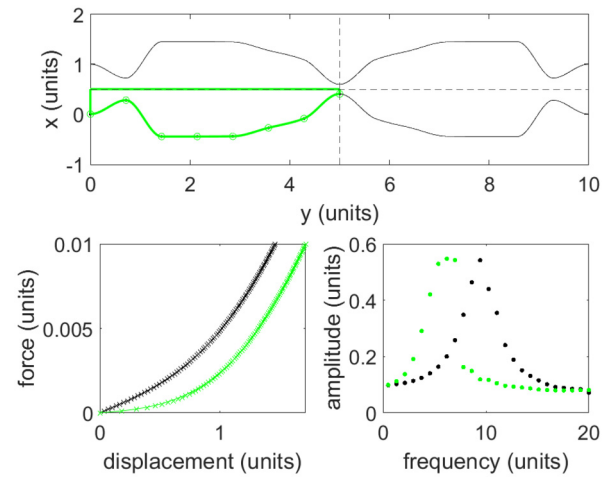

Fig. 8. Optimized nonlinear beam configuration. Top: The nonlinear beam configuration is shown, with control points $a = 0.278$, $b = -0.450$, $c = -0.450$, $d = -0.445$, $e = -0.276$, $f = -0.894$, $g = 0.402$. The green portion represents the quarter of the beam described by these control points, while the rest of the optimized beam is plotted in black. Bottom-left: The force-displacement curve of the nonlinear beam configuration (green) and the rectangular prism beam (black). Bottom-right: The frequency-amplitude response of the nonlinear beam configuration (green) and the rectangular beam (black), when the forcing amplitude is set to 0.4. Notice that the nonlinear beam configuration has a noticeable jump in the frequency-amplitude plot, while the rectangular prism beam does not. In the lower left plot, the Xs correspond to numerical results, and the solid curve corresponds to the curve fit.

4.2. Nonlinear beam configuration

When minimizing the objective function found in Eq (9), the topology optimization procedure produces the beam shape found in Fig. 8. Using the nonlinear objective function, there was a 0.051% improvement from generation 4 to generation 5. This nonlinear beam configuration is shown in the top portion of Fig. 8. The force-displacement curve is shown in the bottom-left portion of this figure. For the rectangular prism beam, $k_1 = 0.0030$ and $k_3 = 0.0018$. For the nonlinear beam configuration, $k_1 = 0.0006$ and $k_3 = 0.0018$. In this case, the cubic stiffness term stayed almost the same as the rectangular prism case, while the linear stiffness term decreased considerably.

In Fig. 8, the dynamic forcing amplitude was set to $a = 0.01$; for this small amplitude, the rectangular beam has no noticeable jumps. This is expected, since the nonlinear terms can be ignored for such small amplitudes. However, the nonlinear beam configuration, even for this small amplitude of forcing, does exhibit a jump in the amplitude as the frequency is changed at approximately 7 rad/s.

5. Conclusions

The shape optimization procedure presented in this paper is a general method to optimize the nonlinear response of continuous system, without the necessity of analyzing nonlinear normal modes. This method could be used for systems that do not lend themselves to nonlinear normal mode analysis. As an example, a clamped-clamped beam was optimized to have a desired response.

By first using the force-displacement curve fit, a beam was produced that was either more nonlinear or less nonlinear than its rectangular prism counterpart. This procedure was shown to create beams that have strong amplitude dependence. The linear beam configuration (with spring stiffnesses $k_1 = 0.0038$ and $k_3 = 0.0027$) was linear for much higher amplitudes than its rectangular prism counterpart (with spring stiffnesses $k_1 = 0.0030$ and $k_3 = 0.0018$), as no noticeable jump was found in its frequency response curve. The nonlinear beam configuration (with spring stiffnesses $k_1 = 0.0006$ and $k_3 = 0.0018$) was nonlinear

for much smaller amplitudes than its rectangular prism counterpart, as a noticeable jump was found in its frequency response curve even when none was present for the rectangular prism beam.

The beam is constructed with fabricability in mind. The spline used here avoids overshoot. Additionally, there are no sharp edges, because of the choice to set a zero slope condition on the clamped end of the beam and at the center, since the beam is created by reflection about a vertical axis at the center. Without changing the objective functions, the resulting beam shapes found from this study could be physically implemented to have any desired natural frequency by using materials with a specific modulus of elasticity or by changing the thickness of the beam. If a specific material was desired a priori to the optimization, the objective functions themselves could be modified to include the natural frequency as well, though this would likely have some effect on the achieved nonlinearity as well.

Declarations

Author contribution statement

Tushar Mollik: Conceived and designed the experiments; Performed the experiments; Analyzed and interpreted the data; Wrote the paper. **Ying Geng:** Conceived and designed the experiments; Performed the experiments; Analyzed and interpreted the data. **Md Raf E Ul Shougat:** Conceived and designed the experiments; Analyzed and interpreted the data. **Timothy Fitzgerald:** Conceived and designed the experiments; Analyzed and interpreted the data; Contributed reagents, materials, analysis tools or data; Wrote the paper. **Edmon Perkins:** Conceived and designed the experiments; Analyzed and interpreted the data; Wrote the paper.

Data availability statement

Data associated with this study has been deposited at https://figshare.com/projects/Genetic_algorithm_shape_optimization_to_manipulate_nonlinear_responses/122785.

Declaration of interests statement

The authors declare no conflict of interest.

References

[1] F. Cottone, H. Vocca, L. Gammaitoni, Nonlinear energy harvesting, Phys. Rev. Lett. 102 (8) (2009) 080601.

[2] S.C. Stanton, C.C. McGehee, B.P. Mann, Nonlinear dynamics for broadband energy harvesting: investigation of a bistable piezoelectric inertial generator, Phys. D: Nonlinear Phenom. 239 (10) (2010) 640–653.

[3] R.E. Mirollo, S.H. Strogatz, Synchronization of pulse-coupled biological oscillators, SIAM J. Appl. Math. 50 (6) (1990) 1645–1662.

[4] J.C. Coulombe, M.C. York, J. Sylvestre, Computing with networks of nonlinear mechanical oscillators, PLoS ONE 12 (6) (2017) e0178663.

[5] E. Collin, Y.M. Bunkov, H. Godfrin, Addressing geometric nonlinearities with cantilever microelectromechanical systems: beyond the duffing model, Phys. Rev. B 82 (23) (2010) 235416.

[6] H. Westra, M. Poot, H. Van Der Zant, W. Venstra, Nonlinear modal interactions in clamped-clamped mechanical resonators, Phys. Rev. Lett. 105 (11) (2010) 117205.

[7] F. Mangussi, D.H. Zanette, Internal resonance in a vibrating beam: a zoo of nonlinear resonance peaks, PLoS ONE 11 (9) (2016) e0162365.

[8] C.-M. Chin, A.H. Nayfeh, Three-to-one internal resonances in parametrically excited hinged-clamped beams, Nonlinear Dyn. 20 (2) (1999) 131–158.

[9] G. Kazakis, I. Kanellopoulos, S. Sotiropoulos, N.D. Lagaros, Topology optimization aided structural design: interpretation, computational aspects and 3d printing, Heliyon 3 (10) (2017) e00431.

[10] M.P. Bendsøe, N. Kikuchi, Generating optimal topologies in structural design using a homogenization method, Comput. Methods Appl. Mech. Eng. 71 (2) (1988) 197–224.

[11] P. Hajela, E. Lee, Genetic algorithms in truss topological optimization, Int. J. Solids Struct. 32 (22) (1995) 3341–3357.

[12] S. Rajan, Sizing, shape, and topology design optimization of trusses using genetic algorithm, J. Struct. Eng. 121 (10) (1995) 1480–1487.

[13] M.P. Bendsøe, A. Ben-Tal, J. Zowe, Optimization methods for truss geometry and topology design, Struct. Optim. 7 (3) (1994) 141–159.

[14] M. Ohsaki, Genetic algorithm for topology optimization of trusses, Comput. Struct. 57 (2) (1995) 219–225.

[15] T.E. Bruns, D.A. Tortorelli, Topology optimization of non-linear elastic structures and compliant mechanisms, Comput. Methods Appl. Mech. Eng. 190 (26–27) (2001) 3443–3459.

[16] H.-A. Lee, G.-J. Park, Topology optimization for structures with nonlinear behavior using the equivalent static loads method, J. Mech. Des. 134 (3) (2012).

[17] M.P. Bendsoe, O. Sigmund, Topology Optimization: Theory, Methods, and Applications, Springer Science & Business Media, 2013.

[18] X. Huang, M. Xie, Evolutionary Topology Optimization of Continuum Structures: Methods and Applications, John Wiley & Sons, 2010.

[19] J. Chen, R. Ahmad, H. Suenaga, W. Li, K. Sasaki, M. Swain, Q. Li, Shape optimization for additive manufacturing of removable partial dentures-a new paradigm for prosthetic cad/cam, PLoS ONE 10 (7) (2015) e0132552.

[20] M. Grossard, C. Rotinat-Libersa, N. Chaillet, M. Boukallel, Mechanical and control-oriented design of a monolithic piezoelectric microgripper using a new topological optimization method, IEEE/ASME Trans. Mechatron. 14 (1) (2009) 32–45.

[21] K. Tai, S. Akhtar, Structural topology optimization using a genetic algorithm with a morphological geometric representation scheme, Struct. Multidiscip. Optim. 30 (2) (2005) 113–127.

[22] T. Talaslioglu, Global stability-based design optimization of truss structures using multiple objectives, Sadhana Proc. Eng. Sci. 38 (1) (2013) 37–68.

[23] T. Talaslioglu, Design optimization of lattice girders according to member and joint-related design constraints, Adv. Steel Constr. 17 (2) (2021) 181–198.

[24] T. Talaslioglu, Optimal dome design considering member-related design constraints, Front. Struct. Civ. Eng. 13 (5) (2019) 1150–1170.

[25] T. Talaslioglu, Comparison of nonlinear solution techniques named arc-length for the geometrically nonlinear analysis of structural systems, J. Eng. Res. 9 (3B) (2021).

[26] E. Biyikli, A.C. To, Proportional topology optimization: a new non-sensitivity method for solving stress constrained and minimum compliance problems and its implementation in matlab, PLoS ONE 10 (12) (2015) e0145041.

[27] I. Sosnovik, I. Oseledets, Neural networks for topology optimization, Russ. J. Numer. Anal. Math. Model. 34 (4) (2019) 215–223.

[28] X. Lei, C. Liu, Z. Du, W. Zhang, X. Guo, Machine learning-driven real-time topology optimization under moving morphable component-based framework, J. Appl. Mech. 86 (1) (2019) 011004:1.

[29] L. Cheng, X. Liang, E. Belski, X. Wang, J.M. Sietins, S. Ludwick, A. To, Natural frequency optimization of variable-density additive manufactured lattice structure: theory and experimental validation, J. Manuf. Sci. Eng. 140 (10) (2018) 105002.

[30] X. Wang, P. Zhang, S. Ludwick, E. Belski, A.C. To, Natural frequency optimization of 3d printed variable-density honeycomb structure via a homogenization-based approach, Addit. Manuf. 20 (2018) 189–198.

[31] W. Ye, S. Mukherjee, N.C. MacDonald, Optimal shape design of an electrostatic comb drive in microelectromechanical systems, J. Microelectromech. Syst. 7 (1) (1998) 16–26.

[32] C. Guo, G.K. Fedder, A quadratic-shaped-finger comb parametric resonator, J. Micromech. Microeng. 23 (9) (2013) 095007.

[33] J. Liang, X. Zhang, B. Zhu, Nonlinear topology optimization of parallel-grasping microgripper, Precis. Eng. 60 (2019) 152–159.

[34] D. Giannini, N. Aage, F. Braghin, Topology optimization of mems resonators with target eigenfrequencies and modes, Eur. J. Mech. A, Solids 91 (2022) 104352.

[35] K. Maute, D.M. Frangopol, Reliability-based design of mems mechanisms by topology optimization, Comput. Struct. 81 (8–11) (2003) 813–824.

[36] V. Zega, A. Frangi, A. Guercilena, G. Gattere, Analysis of frequency stability and thermoelastic effects for slotted tuning fork mems resonators, Sensors 18 (7) (2018) 2157.

[37] S. Nabavi, L. Zhang, Nonlinear multi-mode wideband piezoelectric mems vibration energy harvester, IEEE Sens. J. 19 (13) (2019) 4837–4848.

[38] J. Zhang, S. Zhu, C. Liu, X. Shen, A two-grid binary level set method for eigenvalue optimization, J. Sci. Comput. 89 (3) (2021) 1–21.

[39] S. Zhu, C. Liu, Q. Wu, Binary level set methods for topology and shape optimization of a two-density inhomogeneous drum, Comput. Methods Appl. Mech. Eng. 199 (45–48) (2010) 2970–2986.

[40] G.H. Yoon, Maximizing the fundamental eigenfrequency of geometrically nonlinear structures by topology optimization based on element connectivity parameterization, Comput. Struct. 88 (1–2) (2010) 120–133.

[41] S. Dou, B.S. Strachan, S.W. Shaw, J.S. Jensen, Structural optimization for nonlinear dynamic response, Philos. Trans. R. Soc. A 373 (2051) (2015) 20140408.

[42] B. Stanford, P. Beran, M. Kurdi, Adjoint sensitivities of time-periodic nonlinear structural dynamics via model reduction, Comput. Struct. 88 (19-20) (2010) 1110–1123.

[43] Y.-I. Kim, G.-J. Park, Nonlinear dynamic response structural optimization using equivalent static loads, Comput. Methods Appl. Mech. Eng. 199 (9–12) (2010) 660–676.

[44] S. Dou, J.S. Jensen, Optimization of nonlinear structural resonance using the incremental harmonic balance method, J. Sound Vib. 334 (2015) 239–254.

[45] L.L. Li, P.M. Polunin, S. Dou, O. Shoshani, B. Scott Strachan, J.S. Jensen, S.W. Shaw, K.L. Turner, Tailoring the nonlinear response of mems resonators using shape optimization, Appl. Phys. Lett. 110 (8) (2017) 081902.

[46] T.J.R. Hughes, The Finite Element Method: Linear Static and Dynamic Finite Element Analysis, Dover, 2000.

[47] T. Belytschko, W.K. Liu, B. Moran, K. Elkhodary, Nonlinear Finite Elements for Continua and Structures, 2nd edition, John Wiley & Sons, 2013.

[48] C. Geuzaine, J.-F. Remacle Gmsh, A 3-d finite element mesh generator with built-in pre- and post-processing facilities, Int. J. Numer. Methods Eng. 79 (11) (2009) 1309–1331.

[49] P.F. Pai, A.N. Palazotto, J.M. Greer, Polar decomposition and appropriate strains and stresses for nonlinear structural analyses, Comput. Struct. 66 (6) (1998) 823–840.

[50] P. Pai, Highly Flexible Structures: Modeling, Computation, and Experimentation, American Institute of Aeronautics and Astronautics, 2007.

[51] G.A. Holzapfel, Nonlinear Solid Mechanics: A Continuum Approach for Engineering, Wiley, 2000.

[52] R. Ogden, Non-Linear Elastic Deformations, Dover, 2013.

[53] Y.-C. Chen, L. Wheeler, Derivatives of the stretch and rotation tensors, J. Elast. 32 (3) (1993) 175–182.

[54] J. Chung, G.M. Hulbert, A time integration algorithm for structural dynamics with improved numerical dissipation: the generalized-α method, J. Appl. Mech. 60 (2) (1993) 371–375.

[55] D. Kuhl, E. Ramm, Constraint energy momentum algorithm and its application to non-linear dynamics of shells, Comput. Methods Appl. Mech. Eng. 136 (3–4) (1996) 293–315.

[56] D. Kuhl, M.A. Crisfield, Energy-conserving and decaying algorithms in non-linear structural dynamics, Int. J. Numer. Methods Eng. 45 (5) (1999) 569–599.

[57] S. Erlicher, L. Bonaventura, O.S. Bursi, The analysis of the generalized-α method for non-linear dynamic problems, Comput. Mech. 28 (2) (2002) 83–104.

[58] E. Perkins, Effects of noise on the frequency response of the monostable duffing oscillator, Phys. Lett. A 381 (11) (2017) 1009–1013.